ADVANCED FUNCTIONAL MATERIALS
www.afm-journal.de

Inter-Layer Diffusion of Excitations in 2D Perovskites Revealed by Photoluminescence Reabsorption

Jiaxing Du, Marcello Righetto, Manuel Kober-Czerny, Siyu Yan, Karim A. Elmestekawy, Henry J. Snaith, Michael B. Johnston, and Laura M. Herz**

2D lead halide perovskites (2DPs) offer chemical compatibility with 3D perovskites and enhanced stability, which are attractive for applications in photovoltaic and light-emitting devices. However, such lowered structural dimensionality causes increased excitonic effects and highly anisotropic charge-carrier transport. Determining the diffusivity of excitations, in particular for out-of-plane or inter-layer transport, is therefore crucial, yet challenging to achieve. Here, an effective method is demonstrated for monitoring inter-layer diffusion of photoexcitations in $(PEA)_2PbI_4$ thin films by tracking time-dependent changes in photoluminescence spectra induced by photon reabsorption effects. Selective photoexcitation from either substrate- or air-side of the films reveals differences in diffusion dynamics encountered through the film profile. Time-dependent diffusion coefficients are extracted from spectral dynamics through a 1D diffusion model coupled with an interference correction for refractive index variations arising from the strong excitonic resonance of 2DPs. Such analysis, together with structural probes, shows that minute misalignment of 2DPs planes occurs at distances far from the substrate, where efficient in-plane transport consequently overshadows the less efficient out-of-plane transport in the direction perpendicular to the substrate. Through detailed analysis, a low out-of-plane excitation diffusion coefficient of $(0.26 \pm 0.03) \times 10^{-4}$ cm^2 s^{-1} is determined, consistent with a diffusion anisotropy of ≈4 orders of magnitude.

1. Introduction

In recent years, metal halide perovskites (MHPs) have garnered significant attention owing to their outstanding performance in thin-film solar cells and a broad range of other applications. Power conversion efficiencies of lab-scale perovskite solar cells now match those of the very best silicon solar cells, and frequently exceed 26%.[1] Such remarkable performance is enabled by the excellent optoelectronic properties of MHPs, including high charge-carrier mobility, strong absorption coefficients, and low density of detrimental defects, which – coupled with the large bandgap tunability and low cost for device preparation – has created a new paradigm for thin-film solar cells.[2–7] To date, the material and operational instability of thin-film solar cells based on such bulk, 3D MHP semiconductors therefore remain the only significant technical hurdle to their commercial success.[8,9]

To improve the stability of perovskite solar cells, layered 2D perovskites (2DPs) have been blended and interfaced with 3D MHPs, thereby resulting in improved defect passivation and enhanced stability under humid-air conditions.[10,11] The structure of 2DPs comprises alternated perovskite octahedral inorganic layers and hydrophobic large cation layers, giving rise to a 2D stacked structure.[12,13] The enhanced chemical stability of 2DPs can be attributed to their hydrophobic large cations, which shield the 3D MHPs structure from moisture.[14,15] However, these large cations also fundamentally reshape charge-carrier interactions in 2DPs with respect to their 3D perovskite (3DP) counterparts, through electronic and dielectric confinement effects, resulting in exciton binding energies in excess of 200 meV.[13,16] Furthermore, the layered structure of 2DPs imparts strongly anisotropic optoelectronic properties, and may hinder the movement of charge carriers in the direction perpendicular to the 2D perovskite planes, but the degree of anisotropy is still strongly debated in the literature.[17,18] These novel properties of 2DPs have in turn proven promising for alternative applications in light-emitting diodes and lasers,[19,20] as well as in polarization optical devices.[21] However, for both solar cell device and light-emitting diode operation, their anisotropic charge-carrier transport

J. Du, M. Righetto, M. Kober-Czerny, S. Yan, K. A. Elmestekawy,
H. J. Snaith, M. B. Johnston, L. M. Herz
Department of Physics
Clarendon Laboratory
University of Oxford
Parks Road, Oxford OX1 3PU, U.K.
E-mail: marcello.righetto@physics.ox.ac.uk; laura.herz@physics.ox.ac.uk

L. M. Herz
Institute for Advanced Study
Technical University of Munich
Lichtenbergstrasse 2a, D-85748 Garching, Germany

The ORCID identification number(s) for the author(s) of this article can be found under https://doi.org/10.1002/adfm.202421817

DOI: 10.1002/adfm.202421817

properties may have a negative impact, thus potentially setting a trade-off between stability and efficiency.

Efficient charge-carrier transport is vital for high-efficiency solar cells in planar heterojunction architectures, in particular in the direction toward charge-collecting electrodes. While free electron-hole pairs dominate the excited-state dynamics of 3D MHPs, the high exciton binding energy in 2DPs, well above the thermal energy at room temperature (≈26 meV), implies that excitons become the dominant photophysical species,[22,23] though recent reports have revealed a free charge-carrier population far in excess of that expected from the simple Saha equation.[24] As a result, conventional spectroscopic measurements of charge-carrier transport, such as optical-pump terahertz-probe (OPTP) or time-resolved microwave conductance (TRMC) measurements, which mostly only probe the mobility and dynamics of the residual free charge carriers in 2DPs, are unable to directly record the majority of photoexcited species in these materials.[24,25] In the past few years, photoluminescence (PL)-based methods detecting radiative processes–such as exciton decay and electron-hole bimolecular recombination–have been developed to track the diffusion of charge carriers. In these methods, charge-carrier diffusion processes are studied by monitoring the time-dependent expansion of the PL emission distribution in real space following a focused excitation using pulsed laser.[26] Here, the diffusion coefficients of excitations in 2DPs are extracted by fits to the measured time-dependent "mean square displacement", based on equations describing population and transport dynamics. Such PL-based methods, however, often fail to capture the anisotropy of excitation diffusion in 2DPs as they are mostly sensitive to the dominant in-plane diffusivity. Recently, Cho et al.[27] proposed a method based on photon reabsorption to track charge-carrier diffusion normal to the plane of thin perovskite films, and found this to be effective for 3DPs. However, the short lifetime of excitons in polycrystalline 2DPs,[28] prevented the extraction of out-of-plane excitation diffusion constants for 2DPs in this study. Therefore, an accurate determination of out-of-plane diffusion coefficient for 2DPs, as well as for other layered materials such as transition metal dichalcogenides and 2D covalent organic frameworks, remains a challenge.

In this work, we investigated out-of-plane diffusion of excitations in thin films of the 2D Ruddlesden–Popper perovskite $(PEA)_2PbI_4$ whose inorganic lead-iodide octahedral layers exhibit strong preferential orientation along the substrate plane. We demonstrate a method to track charge-carrier diffusion based on the spectral changes resulting from reabsorption of PL photons emitted by the 2DP and accurately determine the out-of-plane diffusion coefficient of photoexcitations. We are able to overcome the limitations of short excitation lifetime in polycrystalline 2DPs by implementing time-resolved photon detection based on an intensified charge-coupled device (iCCD) camera capable of measuring full luminescence spectra with high amplification and sensitivity. Crucially, by accessing the full PL spectrum here, as a function of time over the range from 1 to 200 ns, we are able to identify and account for spectral features arising from excitonic resonances and the different refractive indices of materials interfacing either side of the 2DP film. By accurately accounting for these effects through an interference model, we are able to determine the average energy of emitted PL photons as a function of time, which is influenced by photon reabsorption effects and therefore the diffusion of excitations through the film depth profile, for different excitation and detection configurations. We determine the out-of-plane diffusion coefficient of excitations from such data, by developing a model based on the 1D diffusion equation to capture the temporal evolution of the average PL energy. We observe an interesting excitation-configuration-dependent change in diffusion coefficients, which we reveal to be caused by variations in the nanostructural orientation of 2DP planes with respect to the substrate, as a function of film depth. We further highlight the strongly anisotropic nature of transport in 2DPs by comparing the determined out-of-plane diffusion coefficient in $(PEA)_2PbI_4$ with well-established values for in-plane motion in the literature. Such comparisons indicate strongly anisotropic diffusion of photoexcitations in $(PEA)_2PbI_4$ thin films with an anisotropy ratio of almost four orders of magnitude. Our findings further highlight the potential of PL reabsorption methods for the study of out-of-plane diffusion of photoexcitations in layered semiconductors, which allows for fundamental understanding and optimized implementation in macroscopic and nanoscale optoelectronics devices.

2. Results and Discussion

2.1. Principle of Photon Reabsorption

Photoluminescence reabsorption processes have been widely observed to contribute to the excited-state dynamics of 3D and lower-dimensional perovskites.[29,32] In the reabsorption process, a large fraction of the photons emitted as a result of exciton decay or free electron-hole recombination are reabsorbed by the perovskite material itself, rather than escaping through its surface. Such effects are particularly pronounced when the Stokes shift (i.e., the difference in energy between the absorption onset and the PL peak) is small, as the increased spectral overlap makes photon recapture increasingly likely. Crucially, reabsorption preferentially affects photons emitted at the higher-energy end of the PL spectrum – an effect that is enhanced by sharp onsets in the absorption spectrum.[30,33] Therefore, reabsorption processes cause a net spectral redshift of the PL signal that increases as the average position of the emitted photons moves deeper into the film, with respect to the detector. In addition, photon reabsorption extends measured photoluminescence lifetimes as a result of the time delays introduced by reabsorption and subsequent re-emission events.[29,34,35] Crucially, reabsorption is also highly informative about charge-carrier diffusion in a semiconductor. The fact that different spatial distributions of photogenerated charge-carriers, e.g., a distribution peaked near a film surface as opposed to a flatter charge-carrier distribution profile, will experience reabsorption to a different extent has enabled researchers to track charge-carrier diffusion in 3DP thin films in the direction normal to the substrate and film plane.[27,36] For 2DPs with preferential layer orientation parallel to the substrate plane, this method would be ideally suited to determine out-of-plane diffusivity of excitations. However, attempts have so far been inconclusive, possibly owing to the faster recombination of photoexcitations in lower-dimensional perovskites, which necessitates exceptionally high sensitivity of detection if they are to be tracked over the typical time scale of diffusion.

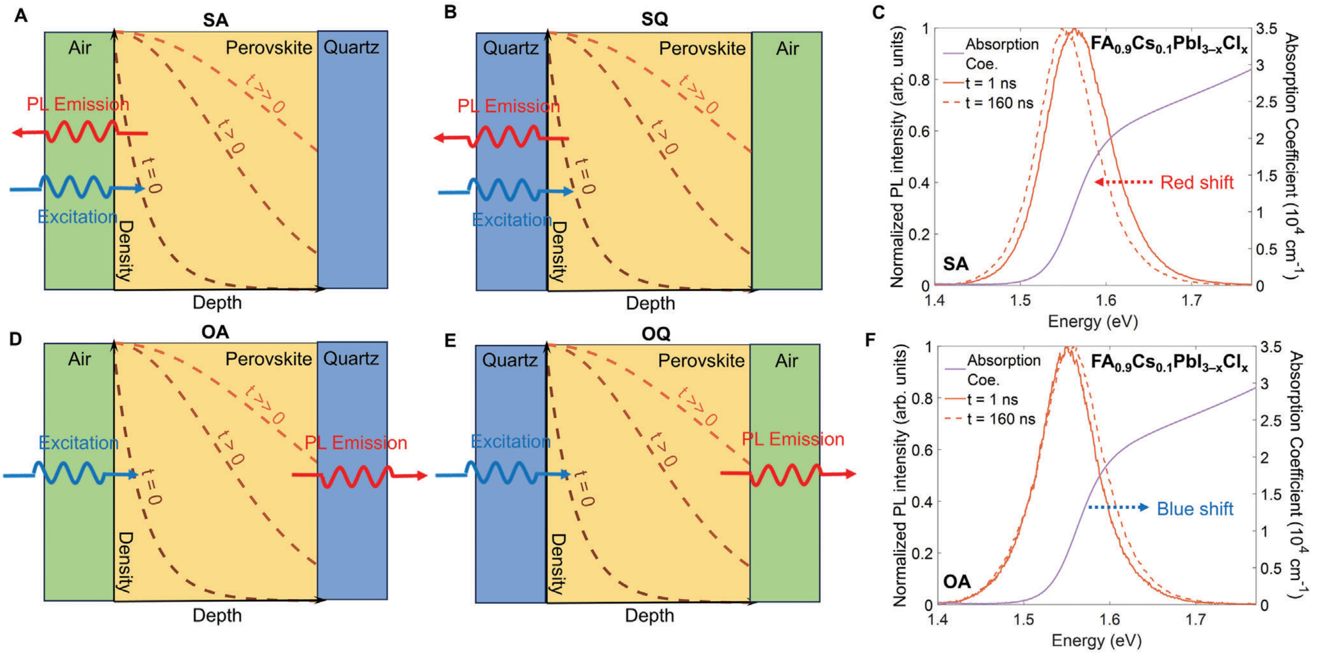

Figure 1. Schematic diagram indicating the different experimental configurations employed in this study: A) same-side collection, air-side excitation (SA), B) same-side collection, quartz-side excitation (SQ), D) opposite-side collection, air-side excitation (OA) and E) opposite-side collection, quartz-side excitation (OQ); Figure highlighting absorption coefficient spectra (purple line) and PL spectra recorded for C) same-side collection and F) opposite-side collection for 3DP $FA_{0.9}Cs_{0.1}PbI_{3\text{-}x}Cl_x$ thin films at the initial time of excitation (1 ns, orange solid line) and at long-time delay (160 ns, orange dashed line), detected by a gated iCCD.

To overcome this hurdle, we here employed an ultrasensitive detection method based on a gated amplified iCCD, allowing us to track vertical (out-of-plane) charge-carrier diffusion in 2DP thin films through time-dependent changes in PL spectra resulting from photon reabsorption processes over a 100 ns time scale. To extract diffusion coefficients from such data, corresponding interference and diffusion models were developed to correct the recorded PL spectra and model their evolution in terms of 1D diffusion of photoexcitations along the film depth profile. These innovations collectively enable a highly powerful method for tracking out-of-plane diffusion of charge carriers in thin films. In our method, we use four different experimental configurations (as illustrated in **Figure** 1A,B and D,E), which differ in the relative orientations of photo-excitation or PL collection with respect to the interface of the 2DP film formed with either air or the quartz substrate. We label these four configurations below as: same-side collection/air-side excitation (SA), opposite-side collection/air-side excitation (OA), same-side collection/quartz-side excitation (SQ) and opposite-side collection/quartz-side excitation (OQ). According to the Beer–Lambert law, photoexcitation with energies higher than the bandgap generates in the film an initial charge-carrier distribution profile that declines exponentially along the depth of the material.[37] Therefore, we note that air-side (SA, OA) and quartz-side (SQ, OQ) excitation scenarios will generate excitation distributions initially located near different film interfaces, which may have consequences for the electronic energy landscapes probed. Furthermore, by contrasting configurations of same-side (SA, SQ) collection with those of opposite-side (OA, OQ) collection we are able to effectively observe the impact of photon reabsorption. For the same-side collection (SA, SQ) configurations (Figure 1A,B), where both photoexcitation and PL collection occurs from the same film side, over time, the initially generated free charge carriers and excitons diffuse deeper into the film and away from the surface. Thus as time progresses, reabsorption effects increase, because the emitted photons must travel a longer distance through the material to reach the detector. This enhanced reabsorption yields an effective redshift of the normalized PL profile with increasing time (Figure 1C), because higher-energy emitted photons are more likely to be reabsorbed than lower-energy photons. In contrast, for opposite-side collection configurations (Figure 1D,E), any PL emitted initially (e.g., at t = 1 ns after excitation) must travel through almost the entire film in order to be detected, hence it experiences considerable reabsorption effects. In this case, charge-carrier diffusion processes away from the initial Beer–Lambert profile will result in reabsorption effects decreasing over time as charge carriers move closer to the collection side. Therefore, opposite-side collection (OA, OQ) configurations should yield blueshifts in recorded PL emission spectra over time (Figure 1F). Here, we record time-dependent PL spectra in all four configurations and track average photon energies in order to capture such redshifts and blueshifts. As a result, we are able to extract clear information about charge-carrier diffusion processes specific to the film interface near which they were initially generated, which also yields information about potential morphological differences along the film profile.

To quantify PL shifts resulting from reabsorption effects, we define and determine an average photon energy $\langle E\rangle$ of the emitted PL (details in Section S4, Supporting Information) as follows:

$$\langle E\rangle = \frac{\int f(E)\, E dE}{\int f(E)\, dE} \tag{1}$$

where $f(E)$ represents the PL lineshape as a function of energy E. Accordingly, a PL blueshift and a PL redshift correspond to increases and decreases in $\langle E\rangle$, respectively. To overcome the limitation caused by the short lifetime of charge carriers and excitons, we utilized an iCCD for detection, which allows for the recording of the full spectra and intensification of the signal therefore enabling the recording of a much larger dynamic range and tracking over longer time delays than is usually possible with more commonly employed time-correlated single photon counting (TCSPC) setups. To illustrate first how such spectra evolve for a prototypical 3DP, Figure 1C–F and Figure S10 (Supporting Information) display transient PL spectra recorded for a thermally evaporated thin film of $FA_{0.9}Cs_{0.1}PbI_{3\text{-}x}Cl_x$ in both SA (Figure 1A) and OA (Figure 1E) configurations, over a time delay range from 1 to 160 ns after pulsed photoexcitation. Here, we maintained the same (air-side) excitation configuration for both detection geometries in order to ensure that the same interface was being probed. For the SA configuration, the average photon energy exhibited an expected redshift (Figure S10, Supporting Information), from 1.568 to 1.556 eV, indicating that higher-energy emissions were indeed increasingly reabsorbed as charge carriers diffused through the film depth profile. Conversely, for OA configurations, the average energy demonstrated a blue shift (Figure S10, Supporting Information) from 1.553 to 1.555 eV, exhibiting an expected reduction in reabsorption effects. Contrasting these average energy dynamics (Figure S10, Supporting Information) shows their convergence and eventual overlap ≈30 ns after photoexcitation, indicating that the diffusion process through the film profile has been completed at this time point, leading to an even profile. Observations of such complete diffusion has previously been made for a 3DP film,[27] however, based on PL transients recorded with TCSPC for either high-or low-energy photon emission. Such TCSPC measurements are viable for 3DPs owing to their long PL lifetime (146 ns; Figure S6, Supporting Information) and relatively high charge-carrier diffusion coefficients (0.08 cm^2s^{-1} for our 3DP investigated here, see Section S7, Supporting Information) compared to 2DPs, and we have thus used these to verify that measurements recorded with either TCSPC or gated iCCD detection yield similar results, as indeed shown in Figures S10–S13 (Supporting Information).

2.2. Exciton Diffusion Tracking in 2DPs

The presence of quantum confinement and dielectric confinement radically alters the nature of Coulomb interactions in layered 2DPs. As a result of this, high exciton binding energies (reaching > 200 meV)[38] yield a stable and dominant population of excitons at room temperature. The Coulomb-correlated nature of excitons may significantly accelerate their recombination, while the reduced dimensionality also accelerates band-to-band recombination of free electrons and holes owing to an enhancement of the density of states near the absorption edge and the reciprocity between absorption and radiative recombination.[28] Therefore, while experimental methods conventionally used to probe diffusion of photoexcitations in 3D semiconductors exhibiting relatively slow recombination are highly effective for tracking the complete process, for 2DP thin films, the faster decay process of photoexcitations (Figures S7–S9, Supporting Information), coupled with their expected slow out-of-plane diffusion, makes such investigations significantly harder.

Here we study exciton diffusion processes in PEA_2PbI_4 2DP films by utilizing a PL reabsorption-based method coupled with high-sensitivity gated detection. The film thickness was measured by a profilometer and further confirmed by absorption measurements and cross-sectional scanning electron microscopy (SEM) (Table S1 and Figures S1–S5, Supporting Information). We note that a film thickness of 110 nm was chosen for most experiments because it approaches the penetration depth l of light at the chosen excitation energy of 3.1 eV (i.e., the inverse of the absorption coefficient, $l = 1/\alpha$) which results in a significant population of photoexcited charge carriers near both interfaces. This condition ideally enhances the sensitivity of our method by yielding a significant PL signal for both same-side (SA/SQ) and opposite side (OA/OQ) configurations and enables us to track the entire diffusion process of excitations, which terminates once a flat depth profile has been reached. We also explored films of thickness above and below this value (270 and 55 nm), which confirm this choice, as discussed further below.

Figure 2A,B illustrate time-dependent PL spectra for a PEA_2PbI_4 2DP thin film, recorded for SA and OA configurations (Figure 2A,B insets) following 3.1-eV excitation with pulses of ≈100 ps duration (details Section S3, Supporting Information). Analogously to what we observed for 3DPs, both SA and OA spectra shift over time to lower and higher energies (SA: red shift; OA: blue shift, see details in Section 2.1), respectively. Again, we interpret these shifts as the signature of the diffusion process through the depth profile of the film. Notably, a slight rise in the normalized PL spectra at photon energies below 2.25 eV was observed for both configurations, likely attributable to emission from low-energy defects or polarons in the 2DP thin films, which has been widely reported.[39,40]

Crucially, given the nanosecond timescale and matching dynamic magnitudes of the respective blue-and red-shifts in average PL energies, these must originate from diffusion of photoexcitations along the film depth profile as transport and recombination typically occur over such timescales.[36] Other possibilities which may cause spectral shifts—such as thermalization (picosecond), and ion migration (microsecond)—are clearly associated with different timescales.[27,36] We note that the layered morphology of 2DP thin films, and in our case, lead-iodide layer orientation parallel to the substrate plane (according analysis presented further below), means that excitations are expected to travel slowly through the film depth profile. Here, the need of excitations to cross planes of near-insulating PEA molecules, means that such out-of-plane diffusion is most likely dominated by dipole-mediated energy transfer mechanisms such as non-radiative Förster resonance energy transfer (FRET) and radiative energy transfer.[33] This structure-induced limitation causes out-of-plane diffusion to be much slower than in-plane diffusion, yet the entire process still happens on the scale of ≈100 nanoseconds.

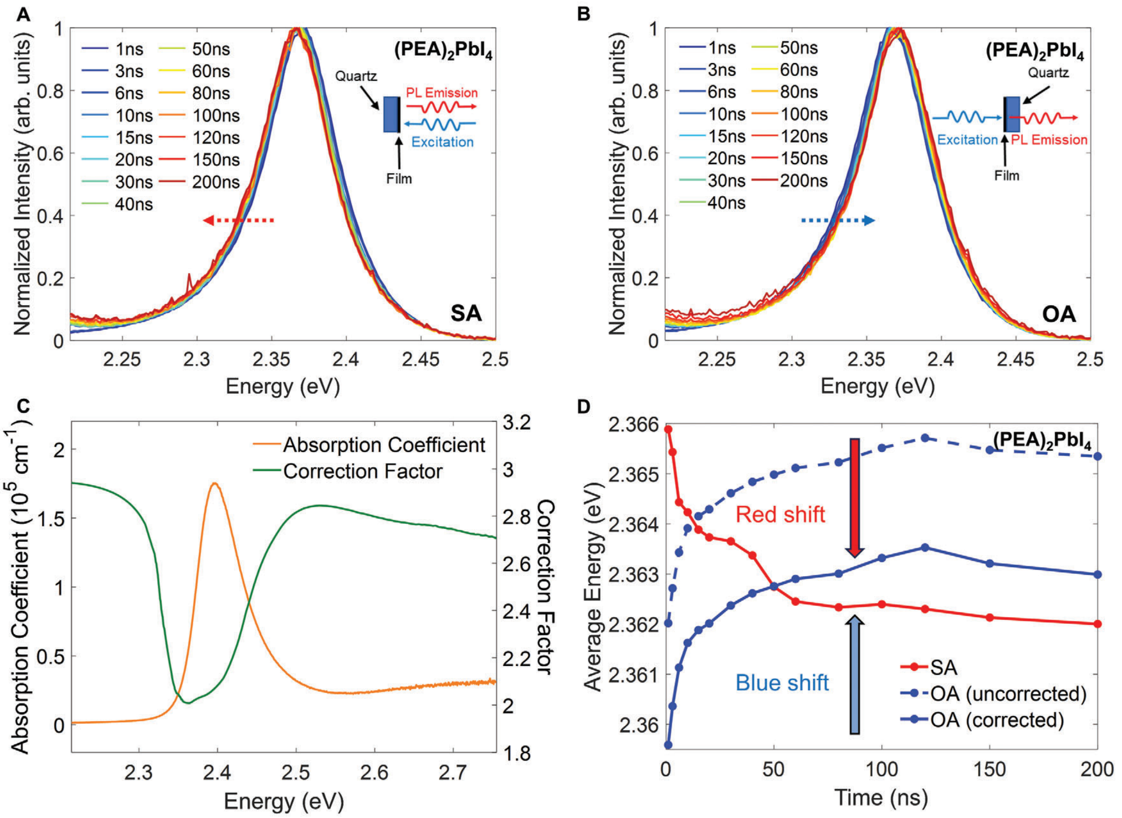

Figure 2. Time-resolved PL spectra for 2DP PEA_2PbI_4 thin films of 110 nm thickness, recorded for A) SA and B) OA configurations over a time delay range from 1 to 200 ns after excitation at 3.1 eV, detected by a gated iCCD and normalized at their peak intensity. The slight rise in the PL spectra at photon energies below 2.25 eV is attributed to emission from low-energy defects or polarons, as previously reported for 2DPs.[39,40] This slight relative rise of low-energy PL leads to the red shift observed in OA curves at longer time delays. Inset schematics illustrate the geometries for SA and OA configurations; C) Correction factor (green line) computed from the interference function and absorption spectra (orange line) for a 110-nm thick PEA_2PbI_4 thin film; D) Average energy of emitted PL photons for SA (red line) and OA configurations (blue solid line for data modified with correction factor, blue dash line for uncorrected data), recorded at times ranging between 1 and 200 ns. The temporal blue and red shifts are indicated by blue and red arrows for OA and SA configurations, respectively.

To quantify the dynamics of this out-of-plane diffusion process in PEA_2PbI_4 thin films, we calculated the average energy of photon emission for OA (blue curve) and SA (red curve) configurations as a function of time from 1 to 200 ns (Figure 2D; Figure S17, Supporting Information). To minimize the impact of the weak low-energy defect emission on these calculations, an energy range from 2.275 to 2.5 eV was selected. We find that the average photon energy for the OA geometry blue shifts from 2.362 to 2.365 eV and stabilizes after ≈100 ns. Conversely, the average energy recorded for the SA geometry red shifts from 2.366 to 2.362 eV and similarly plateaus at 100 ns (see Section 2.1 for details). Intriguingly, despite a careful calculation and exclusion of contributions arising from defect PL, the average energy transients extracted for SA and OA geometries cross each other within tens of nanoseconds and do not converge at long times, thus resulting in PL to emerge at higher energy for the OA than for the SA configuration. This result seems unexpected at first, given that according to our simple reabsorption model, exciton diffusion throughout the film should eventually yield a flat distribution profile of excitations across the film depth profile, at which point both SA and OA configurations should cease to change (as they do) and display the same reabsorption effects and therefore detected photon energies (which they do not). We note that for charge-carrier diffusion in the 3DP film (Figure S10, Supporting Information) discussed above, average photon energies did indeed converge near the same value. Therefore, we posit that this unexpected effect is specific to 2DPs and might arise from their strong excitonic character and the resulting sharp features they exhibit near the absorption onset.

To further elucidate the cause of the observed crossing of the average PL energy curves for 2DPs, we developed an optical interference model (full details provided in Section S6, Supporting Information) to account for transmission through the different film interfaces. Importantly, for photon detection in the SA geometry, the PL emission is collected through the perovskite/air interface, whereas for the OA geometry, it passes through the perovskite/quartz interface. Here, the different refractive index of air and quartz affect the outcoupling of the emitted light, thereby potentially modifying the PL spectrum and hence the average energy of the photons recorded. To account for such effects, we developed a model that applies a correction by accounting for refractive index variations at the different air/perovskite and perovskite/quartz interfaces. The refractive indices of our perovskite thin films were obtained from fits to recorded transmission and reflectance spectra utilizing a transfer matrix method (TMM) (full details provided in Section S5, Supporting Information). By combining the interference model with TMM, we derive an interference function for both cases, i.e., emission spectra recorded through outcoupling from perovskite films to air (IF_{Air}) and to quartz (IF_{Quartz}) (Figures S25 and S26, Supporting Information). To make comparable average energies recorded for the two geometries (OA and SA), we here chose to convert PL emission spectra recorded through quartz to what they would be expected for collection through the air side, using:

$$PL_{\mathrm{Corrected\ OA}}\,(t) = PL_{\mathrm{Uncorrected\ OA}}\,(t) \times \frac{IF_{\mathrm{Air}}}{IF_{\mathrm{Quartz}}} \tag{2}$$

Closer examination of the spectral profile of this correction factor (Figure 2C) further allows us to comment on the reasons why specifically 2DPs exhibits the crossing of curves discussed above. The correction factor displays a pronounced function minimum at ≈2.37 eV which derives from the presence of strong excitonic resonances (Figure 2C) at ≈2.39 eV typical for 2DPs. This effect can be more readily observed by the presence of near-zero transmission (Figure S4, Supporting Information) recorded across the same spectral range. Importantly, the slight deviation between the energy of the absorption peak and the minimum of the correction factor yields a marked effect on wide-angle interference,[41] thus resulting in a distortion of the spectrum. Figure 2D shows how the average PL energy shift of the PEA_2PbI_4 thin film recorded in the OA configuration changes after the correction has been applied. Such correction rigidly shifts the average PL energy to lower energies by 4 meV. As a result, the average PL energy curves for the SA and OA configuration now approach each other, and plateau at ≈100 ns. We note here that, despite correcting for light outcoupling effects, a residual crossing of the average PL energy curve in SA and OA configuration is still observed at ≈50 ns. However, only a very small offset of ≈1 meV is observed in the steady-state limit, suggesting the presence of additional minor factors, such as surface recombination (vide infra), or that our optical model, which does not account for light scattering, does not perfectly replicate the real system. Finally, we note that in the absence of such sharp and strong excitonic resonances near the absorption onset – such as for 3D perovskites – the interference factor is similar to (1-R), where R is reflectance,[42,43] and such spectral distortions will be very minor. As a result, average emission energy trends for such configuration pairs are expected to approach each other without the need for the correction described by Equation (2), as we indeed observe (Figure S10, Supporting Information).

To further validate our approach and the effects of the optical interference correction factor, we measured PL reabsorption dynamics for PEA_2PbI_4 films with different thicknesses (55 and 270 nm), with the results shown in Figure S29 (Supporting Information). We note that a crucial difference between these three cases is the ratio between film thicknesses L and the penetration depth of light ($1/\alpha$) at the excitation energy. The calculated penetration depth of ≈130 nm for 2DPs at 3.1 eV excitation energies is significantly larger than thickness for 55-nm thin films, and significatively smaller than the thickness for 270-nm thin films. Hence, we expect a fairly flat initial distribution of photoexcitations across the film depth profile in the case of the 55-nm thick film, and more sharply peaked distribution at the surface in the case of the 270-nm thick film (Figure S34, Supporting Information). For these two extremes, several challenges arise for tracking of the entire exciton diffusion process: for $L \ll 1/\alpha$, the flat excitation density gradient yields similar photon reabsorption effects on both collection configurations, and therefore, little change is expected to occur over time. On the other hand, for $L \gg 1/\alpha$, recording the complete equilibration process starting from a sharply peaked photoexcitation distribution to one that is flat across the film depth profile is challenging because it could easily approach very long timescales, by which time little emission will be left to detect. We discuss in more detail the interpretation of these cases and the effect of the correction factor in Section S6 (Supporting Information). Overall, we conclude that choosing a film thickness comparable to the penetration depth of the exciting light is ideal for measurements of vertical diffusion of photoexcitations by the photon reabsorption method.

2.3. Extracting Diffusion Coefficients from Simulations

To quantify the PL reabsorption dynamics in the 2DP thin films and extract diffusion coefficients, we simulated the photoexcitation dynamics through a 1D time-dependent diffusion model.[30,44] For this purpose, we assume that the initial distribution of photoexcitations follows the Beer–Lambert law, and subsequent diffusion is captured by the numerical solution to a 1D diffusion equation along the depth profile (Section S7, Supporting Information for full details of the approach). From the excitation depth profile derived for any given time, the anticipated emerging PL spectra were calculated, taking into account the reabsorption effects through the material thickness and the absorption spectrum a photon will encounter when it is emitted at a certain film depth. The average phton energy of the simulated emerging PL spectra was then calculated and compared with actual results derived from experiments. The effects of surface recombination were also taken into account through modified boundary conditions (Section S7, Supporting Information). We first validated the simulation approach by conducting simulations for the $FA_{0.9}Cs_{0.1}PbI_{3\text{-}x}Cl_x$ 3DP films, which yield a diffusion coefficient of $D_{3DP} = 0.08 \pm 0.04\ \mathrm{cm^2 s^{-1}}$ (Figures S32–S38, Supporting Information), in excellent agreement with literature-reported values collected from 3D lead iodide perovskite thin films.[27,45]

We proceed by discussing diffusion simulation results for the PEA_2PbI_4 2DP films. As an example of the simulation capturing the evolving excitation profile, **Figure 3A** shows how the simulated peak of the initial normalized Beer–Lambert photoexcitation distribution slowly moves away from the surface and migrates into the film depth over a 200-ns timescale (here for the SA configuration and a diffusion coefficient of $1.0 \times 10^{-4}\ \mathrm{cm^2\ s^{-1}}$). As expected, the diffusion process progressively flattens the photoexcitation density gradient along the film depth profile, while the extensive surface recombination lowers the contribution from the air side. The change in photoexcitation distribution effectively increases the average distance in the film traveled by emitted photons before they reach a surface, and thus enhances the extent of photon reabsorption.

We found that in general, an additional effect of surface recombination had to be considered when modeling the observed

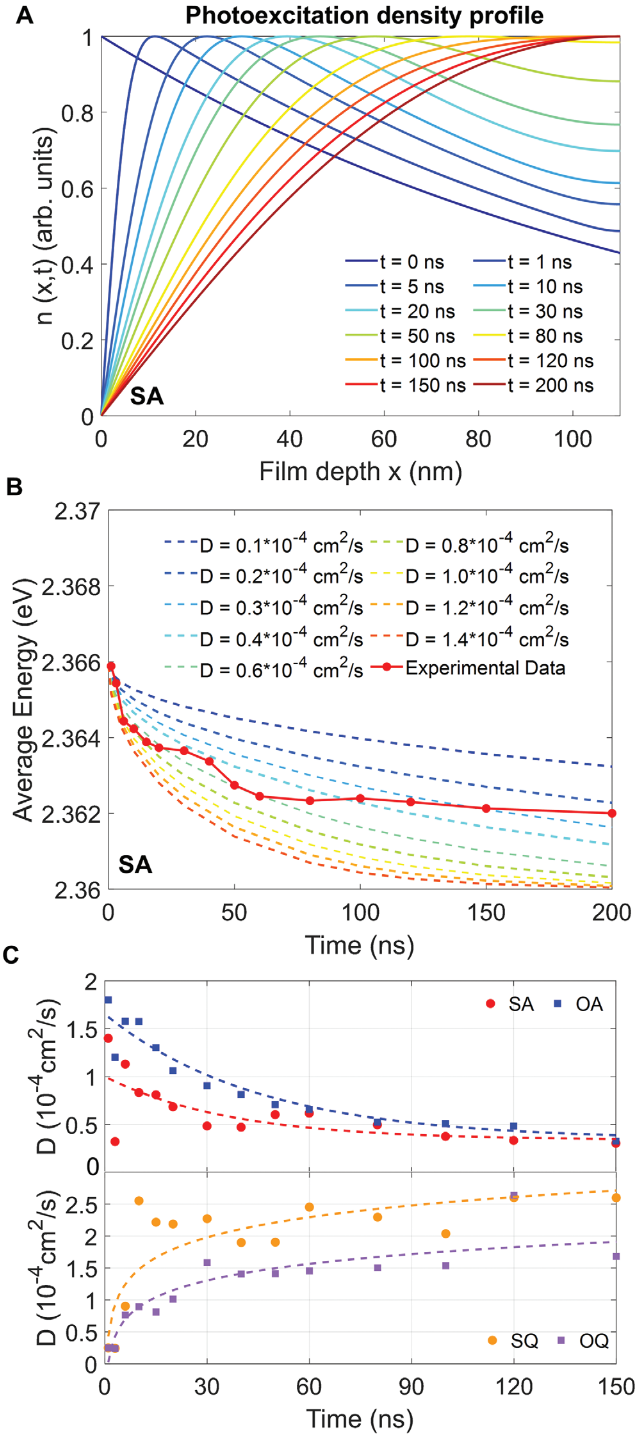

Figure 3. A) Simulated temporal evolution of the photoexcitation density profile, for an assumed diffusion coefficient of 1.0×10^{-4} cm^2 s^{-1} for a 110-nm thick film of the 2DP PEA$_2$PbI$_4$, over a 200-ns timescale following initial photoexcitation, in the SA configuration; B) Dynamic changes in average energy values of detected PL photons, showing simulated values (colored dashed lines) for different diffusion coefficients, together with the experimentally determined values (red circles); C) Diffusion coefficients extracted for all four configurations through comparison and interpolation between experimental data and simulations. Dashed lines are guides to the eye.

peak-energy shifts accurately. In particular, when the two opposite film surfaces (quartz and air interface) exhibit different surface recombination rates, counterintuitive results of PL shifts may be expected, e.g., an SQ blue shift and OQ red shift) (Figure S17 (Supporting Information) for data and Figure S33 (Supporting Information) for simulations for 110 nm-thick PEA$_2$PbI$_4$ 2DP films). Here we find that this observation is related to more defective or disordered material giving rise to higher surface recombination velocities near the film's air-side interface: in simulations reflecting quartz-side excitation, surface recombination generates an "opposite gradient" by rapidly depleting the charge-carrier density near the air-side interface and leads to competition between surface recombination and excitation diffusion. For the OQ geometry (quartz-side excitation) this will lower the number of photons emitted near the opposite side (air side), which will generate a counterintuitive red shift, while for the SQ geometry, a blue shift occurs, when these effects dominate the reabsorption dynamics (Figure S33, Supporting Information). Depending on film thickness and defect density at this air-side interface, either the photon reabsorption effect, or the surface recombination effect therefore dominates the direction of shifts for the quartz-side excitation geometries, with the former being the case for the 270 nm-thick PEA$_2$PbI$_4$ 2DP film and the latter for the 110 nm-thick film (Figure S17, Supporting Information for data and Figure S34, Supporting Information for simulations). We note that for 3DP thin films, the relatively large diffusion coefficient of excitations means that surface recombination cannot cause a strong distortion for the excitation profile, and hence the shift of the PL spectra follows that expected from a simple model based on photon reabsorption alone (Figure S32, Supporting Information). We thus find that our model incorporating exciton diffusion and both bulk and surface-specific recombination can accurately account for the energy peak shifts observed for all four excitation-detection configurations.

We proceed by using such simulations to provide an accurate assessment of the out-of-plane diffusion coefficient for these highly oriented PEA$_2$PbI$_4$ 2DP films. We performed multiple simulations based on diffusion coefficients ranging from 0.1×10^{-4} to 1.4×10^{-4} cm^2 s^{-1}. Figure 3B shows the average photon energy transients calculated for different diffusion coefficients together with those determined experimentally, for the SA configuration. As expected, the curves simulated for a range of diffusion coefficients all start at the same initial emission energy (2.3657 eV) but then decrease with different speed to reach different values at any given time (e.g., between 2.363 and 2.360 eV within the calculated 200-ns time window for diffusion coefficients between 0.1 and 1.4×10^{-4} cm^2 s^{-1}, respectively). The comparison between experimental and calculated average energy transients (red dot line and dotted lines in Figure 3B) reveals that the observed diffusion process does not fully follow any one of these calculated average energy transients. Instead, the experimental data points appear to shift gradually from initially following the curves associated with faster diffusion, to those with lower diffusion coefficients at later times after excitation. To quantify this interesting effect, we extracted a time-dependent diffusion coefficient $D(t)$ from the comparison between data and simulated curves–Figure 3C. Intriguingly, for the SA and OA configurations reflecting air-side excitation of the 110 nm-thick film of PEA$_2$PbI$_4$, the value of the diffusion coefficients monotonically decreases from 1.4 to 0.31×10^{-4} cm^2 s^{-1}, and from 1.8 to 0.32×10^{-4} cm^2 s^{-1}, respectively. In contrast, D(t) values for quartz-side excitation display the opposite trend, i.e., they increase from 0.25 to 2.6×10^{-4} cm^2 s^{-1} for SQ and from 0.24 to 1.6×10^{-4} cm^2 s^{-1} for OQ geometries. We observed that this value is lower than that reported for a single-crystal 2DP[17] which may be caused by the presence of additional grain boundaries present in thin films.[27] These findings reveal that different regions of excitation diffusivity exist in these 2DP films: while the air side of the film supports relatively fast excitation motion in the direction orthogonal to the substrate plane, this motion is significantly slower near the quartz side. Given the highly anisotropic nature of excitation diffusion in 2DPs, we suspect that this effect arises from a slight change in the orientation of 2DP layers across the film depth profile and explore this hypothesis in the next section.

We note that while the diffusion coefficients extracted from the 2DP thin films are significantly lower than those determined for the 3DP thin films, such slower diffusion still results in clearly observable energy shifts within a ≈100 ns window. This effect arises from a multitude of factors influencing the PL energy shifts, including: differing film thicknesses (and an inherent dependence of diffusion timescales on the square root of length scales); differences in magnitude and shape of the absorption coefficient onsets as well as their Stokes shifts with respect to the PL spectrum; and different prominence of surface recombination between the 2D and 3D perovskites. Therefore, the comprehensive modelling undertaken here is essential for an accurate determination of diffusion coefficients from such data.

2.4. Change of Crystalline Orientation

To explore our hypothesis of orientational disorder being present in the 2D structure of the films, we conducted grazing incidence wide-angle X-ray scattering (GIWAXS) measurements with penetration depths ranging from 9 to 150 nm (Figure S40, Supporting Information). The penetration depth was calculated from the corresponding incident angles (Section S8, Supporting Information for details). **Figure 4B** demonstrates how the dispersion along the wide azimuthal direction of the (001) diffraction pattern decreases with increasing penetration depth. Such transitions of the (001) diffraction spot from a more extended "semicircle" shape to a more symmetrical "dot" indicate the narrowing of the distribution of relative orientations of the 2D planes sampled. To quantify this variation, the normalized azimuthal intensity was extracted and plotted in Figure 4C. The significantly reduced diffraction intensity at large azimuthal angle with increasing penetration depth strongly supports the presence of a higher degree of orientational disorder at the air-perovskite interface. Such disorder is reduced closer to the perovskite-quartz interface.

Therefore, the time-dependent diffusion coefficient behavior observed for $(PEA)_2PbI_4$ films may be directly related to the presence of a depth-dependent orientational disorder of the 2D crystalline nanostructure. Specifically, as shown schematically in Figure 4A, we propose that while in proximity of the quartz substrate 2D platelets are highly aligned, this alignment is progressively reduced toward the air-side interface. Such gradual misorientation is likely to occur, given that the predominant ori-

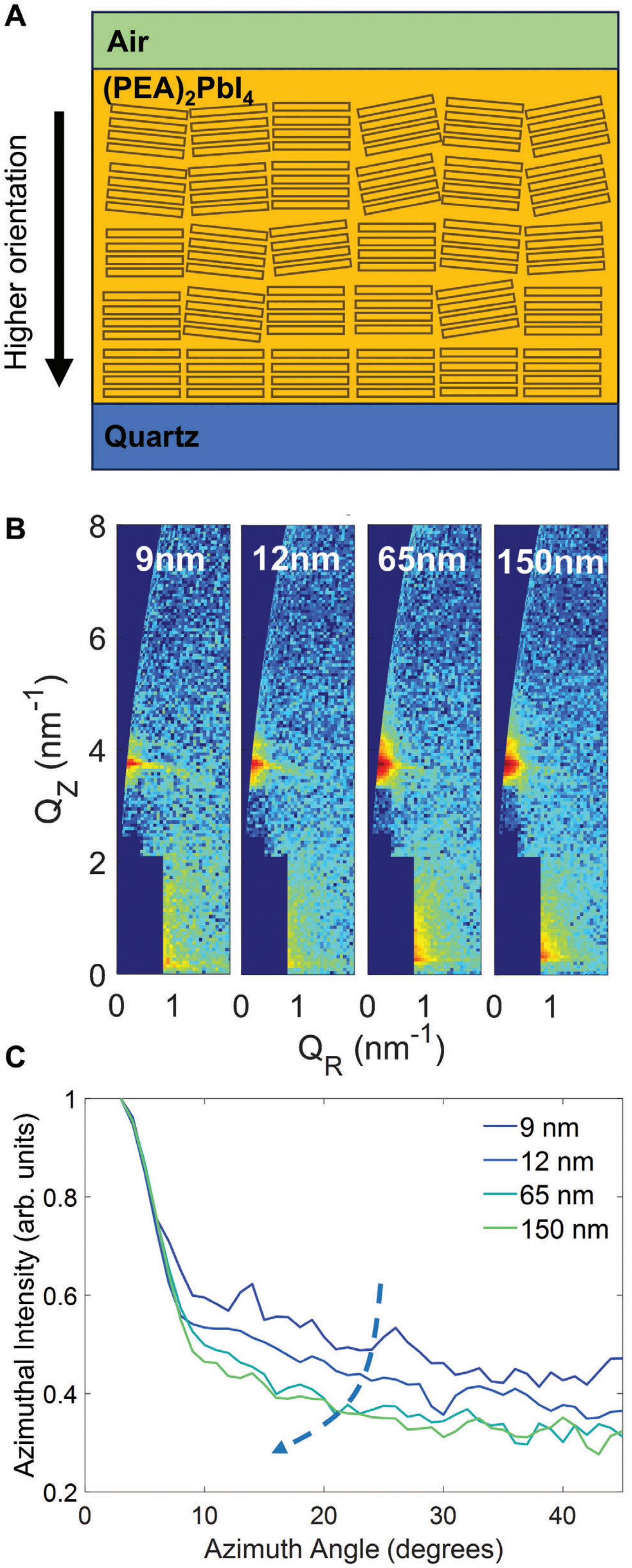

Figure 4. A) Schematic illustrating the change of crystalline layer orientation and nanostructure along a PEA_2PbI_4 film depth profile; B) Depth-dependent GIWAXS images recorded for a 110-nm thick film of 2DP PEA_2PbI_4; C) Azimuthal intensity profiles of the (001) peak for different probe penetration depth.

entation of 2D layers parallel to the substrate is ultimately induced by interactions with the substrate during the casting process and film growth from the substrate upward.[46] The variation in the extracted diffusion coefficients thus emerges as a result of anisotropic charge-carrier diffusion in 2DPs. Exact values for such anisotropy are still debated in literature, but typically represent several orders of magnitude.[18,27,47] Therefore, it is important to note that even slight layer misalignments in the film nanostructure can significantly influence the extracted out-of-plane (oop) diffusion coefficient even if just a small component of in-plane (ip) diffusion is introduced in the vertical orientation.

Our experiments are able to reveal such depth-dependent layer alignments through side-selective excitation of the film, in qualitative agreement with our depth-dependent GIWAXS measurements. Diffusion coefficients extracted from scenarios where most of the charge carriers are situated in the regions closest to the quartz side (SQ and OQ, at early times after excitation) most accurately reflect out-of-plane diffusion (D_{oop}) in highly oriented 2DP films. For air-side excitation measurements (SA and OA) on the other hand, the generated photoexcitation density is initially governed both by oop diffusion (D_{oop}) and ip diffusion within layers exhibiting slight misalignment with respect to the substrate plane ($D_{\text{vertical}-\text{ip}}$). However at later times, when excitations approach the region closer to the substrate, the dynamics transition to predominantly oop diffusion (D_{oop}).

These considerations indicate that in order for the true out-of-plane diffusion coefficient to be determined, the initial values from the quartz-side excitation and the final values from the air-side excitation should be considered, which are indeed very similar (see Figure 4C, for 110-nm thick film) further supporting the reliability of our hypothesis. Taking the mean diffusion coefficient for these conditions, we thus determine the out-of-plane diffusion coefficient for $(\text{PEA})_2\text{PbI}_4$ to be $\text{D}_{2\text{DP}} = (0.26 \pm 0.03) \times 10^{-4}$ $\text{cm}^2\ \text{s}^{-1}$, a value representative of highly oriented 2DPs. We note that for even thicker films (270 nm) such time-dependent diffusion coefficients become even more prominent: air-side excitation reveals an initial diffusion coefficient even larger than that recorded for the 110-nm films (Figure S37, Supporting Information) followed again by a monotonic decrease. This observation again suggests a transition from a combination of ip and oop diffusion to predominantly oop diffusion, this time influenced by even stronger layer misorientation near the air side. These findings further confirm that the orientation distribution broadens as the distance from the substrate increases, reinforcing the relationship between structural misorientation and excitation diffusion in 2DP thin films.

In order to determine a photoexcitation diffusion anisotropy coefficient for the PEA_2PbI_4 2DP thin films, we compare the value D_{oop} determined above for out-of-plane diffusion above with those reported for in-plane diffusion D_{ip} in literature, calculating the ratio $a = D_{\text{ip}}/D_{\text{oop}}$. While determination of D_{oop} has been notoriously difficult because of its small value, experimental and geometric challenges, as well as the layer misorientation issues described above, D_{ip} can be measured very readily, for example via the temporal spreading of an initially created lateral excitation spot on a 2DPs within the layer plane. Based on this method, values of $D_{\text{ip}} = 0.192\ \text{cm}^2\ \text{s}^{-1}$ have been reported for PEA_2PbI_4 thin films,[26] and $D_{\text{ip}} = 0.227\ \text{cm}^2\ \text{s}^{-1}$ for PEA_2PbI_4 single crystals. Taking such values into account, we estimate a sizeable anisotropy of $a \approx 7200$–8700 (i.e., nearly 10^4) for predominantly excitonic diffusion in PEA_2PbI_4 thin films. We note that lower anisotropy values have also been reported,[18,47] however, as we show above, even slight layer misalignment can induce significant increases in perceived vertical transport, which means that measured anisotropy ratios often represent lower boundaries. Overall, these findings thus reveal the fascinating dynamics of such interlayer diffusion and their time-dependent dynamics resulting from nanoscale film morphology.

3. Conclusion

In conclusion, we observed the diffusion dynamics of photoexcitations in 2DP $(\text{PEA})_2\text{PbI}_4$ thin films in the direction perpendicular to the substrate. For this purpose, we developed a method based on accurate measurements and modeling of the dynamic spectral shifts observed in the transient PL signal over a 200 ns time range. We demonstrate that these PL shifts derive from photon reabsorption processes in the thin films and exploit them to estimate the out-of-plane diffusion coefficient for such 2DPs. Our model describes the full dynamics of such effects, resulting from the evolution of the photoexcitation distribution profile from an initial Beer–Lambert profile peaked at the excitation surface to an equilibrated flat distribution, which is attained over a ≈100 ns time window. To quantify these dynamics, we extract an average photon emission energy from PL spectra and track its evolution over time. Crucially, our method relies on four excitation and detection configurations, and is therefore capable of probing different interfaces, e.g. of the film with either the substrate or air as a result of the high absorption coefficient of 2DPs. By comparing these excitation and detection configurations, we identified differences in surface recombination velocities and changes in layer alignment along the film profile, demonstrating that this method effectively reveals variations in material quality along a film depth profile and at its interfaces. Furthermore, we demonstrate that strong spectral modulation deriving from the prominent excitonic peaks near the absorption onset of 2DPs must be accounted for and corrected through a transfer matrix methods approach. Our modelling of the vertical diffusion of photoexcitations, based on a 1D diffusion equation paired with surface recombination boundary conditions, reveal a significant time dependence in the estimated diffusion coefficient. We reveal this to result from depth-dependent orientational disorder encountered in 2DP films, i.e., a misalignment of 2D perovskite planes with respect to the substrate. Coupled with the highly anisotropic transport properties of such 2DPs, even the presence of slight misalignment causes contributions from highly efficient in-plane transport to overshadow the less efficient out-of-plane transport. The resulting evolution in the diffusion coefficient is therefore attributed to changes in the degree of orientational disorder encountered along the film profile, confirmed by depth-dependent GIWAXS measurements. By isolating these effects, we determine the out-of-plane diffusion coefficient of $(\text{PEA})_2\text{PbI}_4$ to be $(0.26 \pm 0.03) \times 10^{-4}\ \text{cm}^2\text{s}^{-1}$, representing a significant diffusion anisotropy of ≈8000 for photoexcitations. Overall, our findings highlight the significant potential of 2DP thin films as anisotropic optoelectronic materials and provide crucial assessment of out-of-plane diffusion of photoexcitations, which have significant impact on the design of high-performance optoelectronic and nanoscopic device structures.

Supporting Information

Supporting Information is available from the Wiley Online Library or from the author.

Acknowledgements

The authors gratefully acknowledge funding from the Engineering and Physics Sciences Research Council (EPSRC) UK. K.A.E. acknowledges the support of the Rank Prize through a Return to Research grant. L.M.H. acknowledges support through a Hans Fischer Senior Fellowship from the Technical University of Munich's Institute for Advanced Study, funded by the German Excellence Initiative.

Conflict of Interest

Henry Snaith is cofounder and CSO of Oxford PV Ltd, a company commercializing perovskite PV technology.

Data Availability Statement

The data that support the findings of this study are available from the corresponding author upon reasonable request.

Keywords

2D perovskites, anisotropy, diffusion, photoluminescence, photon reabsorption

Received: November 11, 2024
Revised: January 17, 2025
Published online: February 16, 2025

[1] Z. Liang, Y. Zhang, H. Xu, W. Chen, B. Liu, J. Zhang, H. Zhang, Z. Wang, D.-H. Kang, J. Zeng, X. Gao, Q. Wang, H. Hu, H. Zhou, X. Cai, X. Tian, P. Reiss, B. Xu, T. Kirchartz, Z. Xiao, S. Dai, N.-G. Park, J. Ye, X. Pan, *Nature* **2023**, *624*, 557.
[2] L. M. Herz, *ACS Energy Lett.* **2017**, *2*, 1539.
[3] L. M. Herz, *Annu. Rev. Phys. Chem.* **2016**, *67*, 65.
[4] M. A. Green, A. Ho-Baillie, H. J. Snaith, *Nat. Photonics* **2014**, *8*, 506.
[5] K. J. Savill, A. M. Ulatowski, M. D. Farrar, M. B. Johnston, H. J. Snaith, L. M. Herz, *Adv. Funct. Mater.* **2020**, *30*, 2005594.
[6] Y. Gong, S. Yue, Y. Liang, W. Du, T. Bian, C. Jiang, X. Bao, S. Zhang, M. Long, G. Zhou, J. Yin, S. Deng, Q. Zhang, B. Wu, X. Liu, *Nat. Commun.* **2024**, *15*, 1893.
[7] H. Tao, W. Zhang, C. Zhang, L. Han, J. Wang, B. Tan, Y. Li, C. Kan, *Opt. Commun.* **2019**, *443*, 262.
[8] V. J. Y. Lim, A. M. Ulatowski, C. Kamaraki, M. T. Klug, L. M. Perez, M. B. Johnston, L. M. Herz, *Adv. Energy Mater.* **2022**, *13*, 2200847.
[9] A. K. Mishra, R. K. Shukla, *Mater. Today: Proceedings* **2020**, *29*, 836.
[10] Z. Wang, Q. Lin, F. P. Chmiel, N. Sakai, L. M. Herz, H. J. Snaith, *Nat. Energy* **2017**, *2*, 17135.
[11] L. R. V. Buizza, T. W. Crothers, Z. Wang, J. B. Patel, R. L. Milot, H. J. Snaith, M. B. Johnston, L. M. Herz, *Adv. Funct. Mater.* **2019**, *29*, 1902656.
[12] L. Yan, J. Ma, P. Li, S. Zang, L. Han, Y. Zhang, Y. Song, *Adv. Mater.* **2022**, *34*, 2106822.
[13] M. Righetto, D. Giovanni, S. S. Lim, T. C. Sum, *Appl. Phys. Rev.* **2021**, *8*, 011318.
[14] P. Huang, S. Kazim, M. Wang, S. Ahmad, *ACS Energy Lett.* **2019**, *4*, 2960.
[15] W. Fu, H. Liu, X. Shi, L. Zuo, X. Li, A. K. Y. Jen, *Adv. Funct. Mater.* **2019**, *29*, 1900221.
[16] X. Hong, T. Ishihara, A. V. Nurmikko, *Phys. Rev. B* **1992**, *45*, 6961.
[17] X. Lou, Y. Li, H. Lei, Y. Zhang, H. Zhou, E. Shi, H. Zhu, *ACS Nano* **2024**, *18*, 20659.
[18] A. J. Magdaleno, M. Seitz, M. Frising, A. Herranz de la Cruz, A. I. Fernandez-Dominguez, F. Prins, *Mater. Horiz.* **2021**, *8*, 639.
[19] Y. Liang, Q. Shang, Q. Wei, L. Zhao, Z. Liu, J. Shi, Y. Zhong, J. Chen, Y. Gao, M. Li, X. Liu, G. Xing, Q. Zhang, *Adv. Mater.* **2019**, *31*, 1903030.
[20] A. J. Ramadan, W. H. Jeong, R. D. J. Oliver, J. Jiang, A. Dasgupta, Z. Yuan, J. Smith, J. E. Lee, S. G. Motti, O. Gough, Z. Li, L. M. Herz, M. B. Johnston, H. Choi, J. Even, C. Katan, B. R. Lee, H. J. Snaith, *Adv. Funct. Mater.* **2024**, *34*, 2309653.
[21] J. Li, J. Ma, X. Cheng, Z. Liu, Y. Chen, D. Li, *ACS Nano* **2020**, *14*, 2156.
[22] G. Xing, B. Wu, X. Wu, M. Li, B. Du, Q. Wei, J. Guo, E. K. L. Yeow, T. C. Sum, W. Huang, *Nat. Commun.* **2017**, *8*, 14558.
[23] D. Marongiu, M. Saba, F. Quochi, A. Mura, G. Bongiovanni, *J. Mater. Chem. C* **2019**, *7*, 12006.
[24] S. G. Motti, M. Kober-Czerny, M. Righetto, P. Holzhey, J. Smith, H. Kraus, H. J. Snaith, M. B. Johnston, L. M. Herz, *Adv. Funct. Mater.* **2023**, *33*, 2300363.
[25] M. Kober-Czerny, S. G. Motti, P. Holzhey, B. Wenger, J. Lim, L. M. Herz, H. J. Snaith, *Adv. Funct. Mater.* **2022**, *32*, 2203064.
[26] M. Seitz, A. J. Magdaleno, N. Alcazar-Cano, M. Melendez, T. J. Lubbers, S. W. Walraven, S. Pakdel, E. Prada, R. Delgado-Buscalioni, F. Prins, *Nat. Commun.* **2020**, *11*, 2035.
[27] C. Cho, S. Feldmann, K. M. Yeom, Y. W. Jang, S. Kahmann, J. Y. Huang, T. C. Yang, M. N. T. Khayyat, Y. R. Wu, M. Choi, J. H. Noh, S. D. Stranks, N. C. Greenham, *Nat. Mater.* **2022**, *21*, 1388.
[28] R. L. Milot, R. J. Sutton, G. E. Eperon, A. A. Haghighirad, J. Martinez Hardigree, L. Miranda, H. J. Snaith, M. B. Johnston, L. M. Herz, *Nano Lett.* **2016**, *16*, 7001.
[29] H. Diab, C. Arnold, F. Ledee, G. Trippe-Allard, G. Delport, C. Vilar, F. Bretenaker, J. Barjon, J. S. Lauret, E. Deleporte, D. Garrot, *J. Phys. Chem. Lett.* **2017**, *8*, 2977.
[30] Y. Yamada, T. Yamada, Q. P. le, N. Maruyama, H. Nishimura, A. Wakamiya, Y. Murata, Y. Kanemitsu, *J. Am. Chem. Soc.* **2015**, *137*, 10456.
[31] J. B. Patel, A. D. Wright, K. B. Lohmann, K. Peng, C. Q. Xia, J. M. Ball, N. K. Noel, T. W. Crothers, J. Wong-Leung, H. J. Snaith, L. M. Herz, M. B. Johnston, *Adv. Energy Mater.* **2020**, *10*, 2203064.
[32] C. Cho, Y. W. Jang, S. Lee, Y. Vaynzof, M. Choi, J. H. Noh, K. Leo, *Sci. Adv.* **2021**, *7*, eabj1363.
[33] D. Giovanni, M. Righetto, Q. Zhang, J. W. M. Lim, S. Ramesh, T. C. Sum, *Light Sci. Appl.* **2021**, *10*, 2.
[34] Y. Yamada, T. Yamada, Y. Kanemitsu, *Bull. Chem. Soc. Jpn.* **2017**, *90*, 1129.
[35] T. W. Crothers, R. L. Milot, J. B. Patel, E. S. Parrott, J. Schlipf, P. Muller-Buschbaum, M. B. Johnston, L. M. Herz, *Nano Lett.* **2017**, *17*, 5782.
[36] Z. Li, Y. Chen, C. Burda, *J. Phys. Chem. C* **2019**, *123*, 3255.
[37] O. Ilze, S. Janis, *J. Biomed. Opt.* **2021**, *26*, 100901.
[38] Y.-Q. Zhao, Q.-R. Ma, B. Liu, Z.-L. Yu, J. Yang, M-Q. Cai, *Nanoscale* **2018**, *10*, 8677.
[39] X. Wu, M. T. Trinh, D. Niesner, H. Zhu, Z. Norman, J. S. Owen, O. Yaffe, B. J. Kudisch, X. Y. Zhu, *J. Am. Chem. Soc.* **2015**, *137*, 2089.
[40] S. Kahmann, E. K. Tekelenburg, H. Duim, M. E. Kamminga, M. A. Loi, *Nat. Commun.* **2020**, *11*, 2344.
[41] W. Lukosz, *J. Opt. Soc. Am.* **1981**, *71*, 744.

[42] J. K. Larsen, S. Y. Li, J. J. S. Scragg, Y. Ren, C. Hägglund, M. D. Heinemann, S. Kretzschmar, T. Unold, C. Platzer-Björkman, *J. Appl. Phys.* **2015**, *118*, 035307.
[43] R. T. Holm, S. W. McKnight, E. D. Palik, W. Lukosz, *Appl. Opt.* **1982**, *21*, 2512.
[44] M. Feng, S. Ye, Y. Guo, T. C. Sum, *Nano Lett.* **2022**, *22*, 7195.
[45] Z. Guo, J. S. Manser, Y. Wan, P. V. Kamat, L. Huang, *Nat. Commun.* **2015**, *6*, 7471.
[46] S. T. Ha, R. Su, J. Xing, Q. Zhang, Q. Xiong, *Chem. Sci.* **2017**, *8*, 2522.
[47] Z. Shi, Z. Ni, J. Huang, *ACS Energy Lett.* **2022**, *7*, 984.